INTERNATIONAL JOURNAL OF
ENERGY RESEARCH WILEY

Rugae-like N-doped porous carbon incorporated with Fe-N$_x$ and Fe$_3$O$_4$ dual active sites as a powerful oxygen reduction catalyst for zinc-air batteries

Chuan Hu[1] | Caixia Gu[1] | Man Guo[1] | Yan Hu[1] | Jiaxin Dong[1] |
Lawrence D'Souza[2] | Isimjan Tayirjan Taylor[2] | Xiulin Yang[1] ⬤

[1]Guangxi Key Laboratory of Low Carbon Energy Materials, School of Chemistry and Pharmaceutical Sciences, Guangxi Normal University, Guilin, China

[2]Saudi Basic Industries Corporation (SABIC), King Abdullah University of Science and Technology (KAUST), Thuwal, Saudi Arabia

Correspondence
Xiulin Yang and Jiaxin Dong, Guangxi Key Laboratory of Low Carbon Energy Materials, School of Chemistry and Pharmaceutical Sciences, Guangxi Normal University, Guilin 541004, China.
Email: xlyang@gxnu.edu.cn (X. Y.) and chemdjx@gxnu.edu.cn (J. D.)

Isimjan Tayirjan Taylor, Saudi Basic Industries Corporation (SABIC), King Abdullah University of Science and Technology (KAUST), Thuwal 23955-6900, Saudi Arabia.
Email: isimjant@sabic.com

Summary

The sluggish kinetics of an air cathode has limited the wide application of zinc-air batteries. As novel powerful electrocatalysts, atomic Fe-N-C materials have attracted immense research interest. However, creating Fe-N-C and Fe$_3$O$_4$ dual-sites catalysts is still challenging. Here, we employ a facile and raw-material-sparse strategy to construct a zeolitic imidazolate frameworks (ZIF)-8-derived N-doped carbon catalyst configured by embedded Fe-N$_x$-C/Fe$_3$O$_4$ dual sites on highly flexible carbon clothe. By soaking the precursor in the iron solution followed by pyrolysis at an optimized temperature, Fe species can translate into dual sites. Our results reveal that the optimal Fe-NC-950 catalyst displays an impressive quasi-four-electron-transfer oxygen reduction reaction pathway exhibiting half-wave potential ($E_{1/2}$) of 0.89 V and onset potential (E_{onset}) of 1.04 V. Moreover, Fe-NC-950 based zinc-air cell reached a high open-circuit voltage of 1.54 V and a power density of 165.0 mW cm^{-2}. Our results also showed that the trace amount of Zn species inherited from ZIF-8 does not affect the catalyst performance.

KEYWORDS
electrocatalysis, Fe$_3$O$_4$, Fe-N$_x$, oxygen reduction, ZIF-8, zinc-air batteries

1 | INTRODUCTION

Developing efficient, inexpensive, and sustainable energy storage and conversion devices is of tremendous interest because of the depletion of fossil fuels.[1-4] Among various options, Zinc-air cells are supposed to be one of the favorite candidates owing to their high theoretical specific energy (1218 Wh kg^{-1}), intrinsic safety, and inexpensiveness.[5] The overall efficiency of the batteries, to a great extent, depends on the cathode's oxygen reduction reaction (ORR), which is a vital rate-determining step.[6,7] However, the sluggish kinetics of the ORR require platinum group metals,[8] which are impeded by scarcity, dissatisfied durability, and intolerance to intermediates in wide application. Consequently, the demand for exploiting earth-abundant metal-based catalysts that possess oxygen-sensitive active centers with strong O=O bond splitting capacity, appropriate geometric structure for facilitating the mass transfer, sturdy reactive centers for long-term durability, and excellent resistance to intermediate poisoning is imperative.[9-13]

Since electrochemical reactions occur on the superficial atoms, smaller active sites and more accessible atoms are crucial for enhancing catalytic activity.[14] So far, materials configured M-Nx active sites (primarily single atoms), embedded in carbon support, have caught significant attention.[15-17] Compared with other researched catalysts (eg, carbides, oxides, sulfides), carbon-based catalysts hold excellent stability, good conductivity, large specific surface area, high atom utilization, as well as flexibility with dopants.[18-21] Simultaneously, the single-atom catalysts have nearly 100% atomic utilization.[22] The literature depicts that single metal atoms coordinated with heteroatoms (eg, N) embedding in carbon materials possess excellent ORR activity[23-29] because of the discrepancy in electron spin density electronegativity and the charge polarization between heteroatoms and carbon. The distributions of charges caused by the incorporated metal and heteroatoms improve the adsorption of oxygen and the split of the double O=O bond.[30,31] It is universally accepted that the TM-Nx active centers may also adjust the binding strengths of reaction intermediates (eg, *O$_2$, *OOH, *OH, *O) to the active sites by altering their electronic structures to boost the ORR.[32-35]

Recently, as a sub-category of metal-organic framework (MOF), zeolitic imidazolate frameworks (ZIFs) unique surface geometry, ultra-high surface area, large pores, and structural flexibility made it a suitable precursor for manufacturing structurally customized carbon-based materials.[36] Previous reports have shown that Fe-N$_x$ active sites own a competitive ORR performance for Pt-based catalysts.[37] A recent ORR activity comparison study on the Fe/N-C showed that the dual-sited Fe/Fe$_3$O$_4$@N-G possesses the best performance relative to that of Fe$_x$N@N-G and FeC$_3$@N-G.[38] However, the conventional pyrolysis suffers from achieving the uniformly dispersed active sites and performance reproducibility. MOF-derived ORR carbon catalysts were synthesized to overcome these limitations by transforming N-rich MOFs decorated with iron species into Fe-N$_x$-doped carbon materials via pyrolysis.[39] However, directly increasing the Fe precursors content to get sufficient Fe-N$_x$ sites will cause the formation of additional inactive metallic iron and oxides.[40] As a result, optimization is necessary to avoid inactive nanoparticles, meanwhile transforming the Fe precursor into the coexistent active Fe-N$_x$ and oxide moieties. Systematic investigation of the impact of the additional metal component inherited from MOFs such as Zn from ZIFs is critical, which is often neglected.

We adopted an impregnation method to synthesize Fe-doped ZIF precursors in this work. Under optimized conditions, the one-step pyrolysis yielded Fe-N$_x$ and Fe$_3$O$_4$ dual sites embedded Fe-NC-950, which differs from the inevitable formation of the unstable aggregate Fe-containing nanoparticles. Benefiting from the rhombus dodecahedron structure's large pore volumes and large surface areas of ZIF-8, the Fe-NC-950 gains a specific surface area of 1104.4 m^2 g^{-1}, which contributes to afford large electrochemically active surface area (ECSA) and provide more available active centers. The Fe-NC-950 exhibited excellent ORR activity in 0.1 M KOH solution due to the accelerated mass transfer, accessible active centers, and synergies of dual centers. Furthermore, it possesses higher methanol tolerance than commercial Pt/C and outstanding durability with a subtle current attenuation of 3% after 36 000 seconds operation. We also evaluated the impact of the Zn species on the catalyst performance, confirming the negligible effect of the residual Zn species in the catalyst. Interestingly, the zinc-air battery-based Fe-NC-950 achieves a high specific capacity of 786.7 mA h g$_{Zn}$$^{-1}$ and satisfactory longtime stability of 170 hours.

2 | EXPERIMENTAL SECTION

2.1 | Synthesis of catalysts

The ZIF-8 precursor was synthesized by following the literature.[41] Typically, 200 mg of ZIF-8 powder was first dispersed in 20 mL of methanol solution and sonicated for 0.5 hours to form a uniform suspension. Subsequently, 8 mg Fe(NO$_3$)$_3$·9H$_2$O was added, and sonicated for 0.5 hour followed by stirring for 2 hours. Then, 6 mL deionized water containing a few drops of ammonium

hydroxide was added. After stirring for 6 hours, Fe-ZIF-8 was collected by centrifugation and subsequent drying at 60°C for 12 hours. Finally, Fe-ZIF-8 was calcined at 850°C, 950°C, and 1050°C under argon flow for 1 hour (heating rate: 5°C min^{-1}) in a tube furnace. Thus, the obtained materials were labeled as Fe-NC-T (where T stands for calcination temperature). For comparison, NC-950 was also obtained by directly calcining ZIF-8 at 950°C under similar calcination condition. Similarly, Fe-AC-950 was synthesized by replacing ZIF-8 with the same amount of activated carbon.

2.2 | Electrochemical measurements

Preparation of electrocatalyst ink for ORR tests: 1 mg of electrocatalyst powder was dispersed in 395 μL isopropanol mixed with 5 μL of Nafion solution, and sonicated to obtain a homogeneous ink. Ink of Pt/C (20 wt% Pt) was also prepared similarly. Next, 32 and 40 μL electrocatalyst ink were pipetted onto a glassy carbon (GC) rotating disk electrode (RDE) electrode (0.196 cm^2) and GC rotating ring-disk electrode (RRDE) electrode (disk area: 0.247 cm^2, ring area: 0.187 cm^2), respectively. Catalyst loading of both are controlled to get about 0.4 mg cm^{-2}. In contrast, Pt/C electrode preparation was done similarly, but the loading changed to 0.1 mg cm^{-2}. The performance test was conducted by a CHI 760E electrochemical workstation in 0.1 M KOH solution with a three-electrode system. The catalyst electrode was set as a working electrode, graphite rod, and Ag/AgCl (3 M KCl) served as a counter electrode and reference electrode, respectively. Further details are given in Supplementary Material. Catalyst ink for OER tests was prepared similarly as mentioned above. Afterwards, the total ink was dropped onto a piece of carbon cloth (1 × 1 cm^2) and dried naturally (loading: 2 mg cm^{-2}). The carbon cloth was used as the working electrode, saturated calomel electrode served as reference electrode, and graphite rod acted as the counter electrode.

2.3 | Zn-air battery test

Hydrophobic carbon paper was used as an air cathode, which also acts as a catalysts carrier and an electron collector, and a zinc plate serves as an anode. First, 2 mg of the catalyst was dispersed in a mixed solvent composed of 200 μL deionized water, 175 μL isopropanol, and 25 μL nafion solution, and sonicated uniformly. Then, 200 μL of ink was coated onto a treated hydrophobic carbon paper to form about 1 cm^{-2} coating (the loading: ~1 mg cm^{-2}). The Pt/C air cathode was obtained in the

same way. The prepared air cathode and zinc foil were assembled into a simple self-made zinc-air battery, using a 6 M KOH containing 0.2 M Zn(Ac)$_2$ aqueous solution as the electrolyte. All tests were performed at normal temperature and atmospheric pressure. The open-circuit voltage (OCV) and power density are measured by CHI 760E electrochemical workstation, and other tests were performed on the Barrett battery test system.

3 | RESULT AND DISCUSSION

3.1 | Material characterization

The synthesis process of Fe-NC-950 is illustrated in Figure 1A. First, the pristine ZIF-8 was fabricated by using Zn^{2+} as a central ion and 2-methylimidazole as a ligand in methanol solution at ambient condition stirring for 24 hours. Subsequently, the as-prepared ZIF-8 was treated in Fe(NO$_3$)$_3$·9H$_2$O solution to obtain Fe-ZIF-8, where the Fe species can be adsorbed into the micropores of ZIF-8 without structural destruction. Finally, Fe-ZIF-8 was subjected to pyrolysis under flowing Ar to carbonize ZIF-8 to obtain a nitrogen-doped carbon framework, while the active Fe species were dispersed and anchored on it. The pyrolysis temperature ranged from 850 to 1050°C to get the optimal catalyst (eg, pyrolysis at 950°C is denoted as Fe-NC-950).

The iron and carbon crystal structure of the material was determined by powder X-ray diffraction (XRD) measurements. The pristine ZIF-8 pattern was identified with the simulated pattern, demonstrating the successful synthesis of the ZIF-8 (Figure S1). After immersing in the Fe(NO$_3$)$_3$ solution, the diffraction peaks of the Fe-ZIF-8 product are the same as that of ZIF-8, indicating that the loading of Fe species did not destroy the crystal structure of ZIF-8. After pyrolysis, the Fe-NC-950 and NC-950 show typical broad peaks at about 25° and 44°, belonging to the (002) and (101) planes of graphitic carbon,[42] which proved that the hydrocarbon network in the ZIF crystal had been completely carbonized (Figure 1B). In addition, several additional diffraction peaks appeared in the Fe-NC-950 sample, which was consistent with the magnetic cubic structure of Fe$_3$O$_4$ (JCPDS: 19-0629).[43] As a control, the XRD patterns of Fe-ZIF-8 calcined at 850°C and 1050°C were measured (Figure S2). The diffraction patterns of Fe-NC-850 contained characteristic peaks of carbon, while the crystallized Fe$_2$O$_3$ (JCPDS: 54-0489), FeO (JCPDS: 49-1447), and Fe (JCPDS: 50-1275) components were detected in Fe-NC-1050, showing that the lower pyrolysis temperature was not beneficial to the formation of crystallized iron particles, but the too high temperature complicates the crystallized iron components, due to the

FIGURE 1 A, Synthetic scheme of Fe-NC-950. B, X-ray diffraction patterns of Fe-NC-950 and NC-950. Scanning electron spectroscopy images of C, ZIF-8, D, Fe-ZIF-8, and E, Fe-NC-950
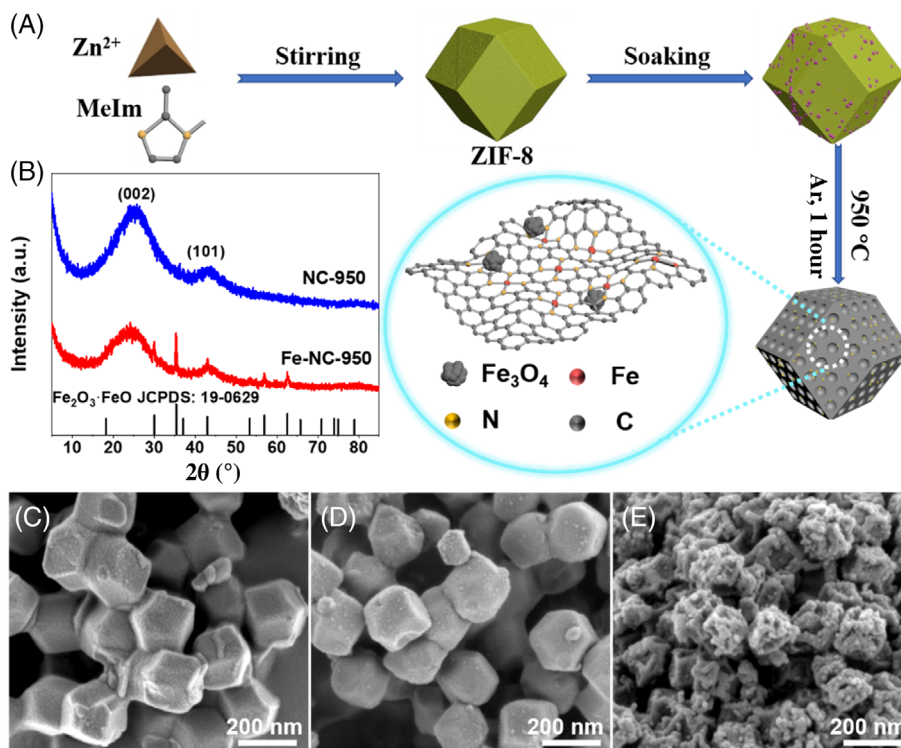
inevitable reduction of iron oxides by carbon sources at higher temperatures (1050°C), resulting in various iron species.[44,45] Besides, the XRD pattern of Fe-AC-950 (Figure S3) showed the characteristic peaks of Fe and Fe_2O_3, respectively.

The microscopic morphology changes are analyzed by scanning electron spectroscopy. The pristine ZIF-8 demonstrated a special rhombic dodecahedron structure without agglomeration, as shown in Figure 1C. It was found that the Fe-ZIF-8 well inherited the original rhombic dodecahedron, suggesting no significant impact of the soaking process on the original morphology (Figure 1D). After pyrolysis, the size of Fe-NC-950 particles had a significant modification due to the pyrolysis induced deformation, and each face became rough and collapsed, but the rhombic dodecahedron structure was intact (Figure 1E). Transmission electron microscopy (TEM) images revealed the particles size of Fe-NC-950 was ca. 100 nm, and the obvious depressions exist on its surface (Figure 2A,B). Selected area electron diffraction revealed the characteristic (400) plane of Fe_3O_4 (Figure 2C). Besides, high-resolution TEM images revealed the crystal lattice spacings of 0.253 and 0.210 nm, corresponding to the (311) and (400) planes of Fe_3O_4 (Figure 2D). This proved that Fe_3O_4 was evenly embedded in the carbon support instead of growing on the surface of the support as aggregated nanoparticles, thereby amplifying the interaction between the carbon supports and improving the structural stability. high-angle annular dark-field-TEM

images and the corresponding energy-dispersive X-ray spectrometry (EDS) mapping revealed the homogeneous dispersion of C, N, O, Fe, as well as a small amount of residual Zn (Figure 2E and Figure S4).

The Brunauer-Emmett-Teller N_2 adsorption and desorption isotherms curve of Fe-NC-950 displayed a Type-IV isotherm characteristic of micro/mesoporous materials (Figure 2F).[46] The pore size distribution curve confirmed the dominant presence of micropores of size less than 2 nm and mesoporous with a size of 3.9 nm in Fe-NC-950 (Figure 2F insert), where the micropores might be created by the retention of the porosity in original ZIF-8 and the volatilization of Zn (bp: 907°C).[47] Owing to structural characteristics mentioned above, the specific surface area of Fe-NC-950 reached 1104.4 $m^2\,g^{-1}$.

Raman spectra of Fe-NC-950, NC-950, and Fe-AC-950 as shown in Figure 2G exhibited two peaks at 1340 cm^{-1} (defect-related) and 1580 cm^{-1} (graphitization-related),[48] the corresponding values of D bands to G bands (I_D/I_G) were 0.96, 1.08, and 1.43. The minimum I_D/I_G value of Fe-NC-950 suggested its highest level of graphitization, while the graphitized carbon not only mediates electron transport but also supports Fe-N_x active sites, and even takes part in ORR as a part of active sites.[49] The mesoporous characteristic is the main factor responsible for the larger specific surface area of Fe-NC-950. In contrast, the ratio of I_D/I_G is origin from the characteristic molecular structure. In addition, the presence of Fe species may increase the degree of graphitization of Fe-NC-950,
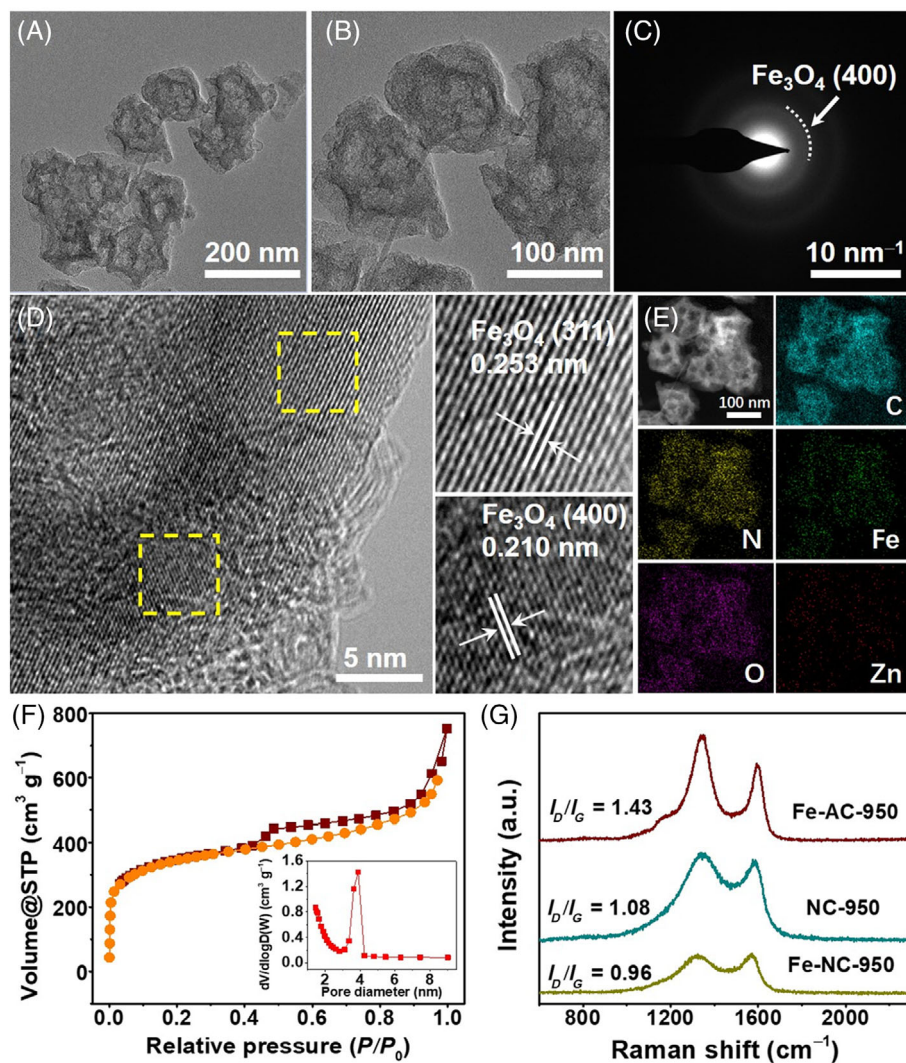
resulting in a smaller I_D/I_G value, which is consistent with the results reported in related reports.[50,51] The lower I_D/I_G value indicates the more ordered graphitic domains (or higher graphitization degree), which favors high electrical conductivity in electrocatalytic processes.[52] Moreover, some studies on Fe-N-C materials suggest that the higher graphitization degree is expected to enhance the overall electronic conductivity and reduce the energy barrier for ORR catalysis.[50,53-56] For Fe-NC-950, Fe_3O_4 species and Fe-N_x sites are supported on carbon supports; the good electronic conductivity of the support is indeed beneficial for ORR. Certainly, extensive reports have demonstrated that defects can promote the oxygen reduction reaction because the introduction of defects in the carbon framework can break the neutrality and redistribute the charges to facilitate the ORR process.[57-61] Therefore, high or low I_D/I_G values represent different structural features of carbon materials, exhibiting different outcomes among various materials.

The chemical valence and surface electronic states of Fe-NC-950 were further unraveled by X-ray photoelectron spectroscopy (XPS) measurement. As shown in Figure 3A, the XPS survey spectra manifested C, N, O, and Fe in Fe-NC-950. The high-resolution C 1s spectrum was deconvoluted into several subpeaks corresponding to C=C (284.0 eV), C—C/C—N (284.8 eV), C—O (286.0 eV), C=O/O-C=O (288.7 eV) (Figure 3B). The success of N doping into carbon matrix was verified by the C—N bond.[62] High-resolution N 1s spectrum displayed four component peaks at 397.8 (pyridinic N, 48.78%), 399.1 (Fe-N_x, 9.80%),[63,64] 400.2 (pyrrolic N, 29.13%), 401.8 eV (graphitic N, 8.85%), and 403.5 eV (oxidized N, 3.44%), proving that N was successfully doped into the carbon skeletons (Figure 3C).[65] By coordinating with pyridine- and pyrrole-N, Fe can form atomically dispersed Fe-N_x species. The coordination of single Fe atoms and the neighboring N was confirmed by the Fe-N bond.[64] The pyridinic N can boost surface wettability[66] and onset potential,[29,67,68] which is vital for enhancing the
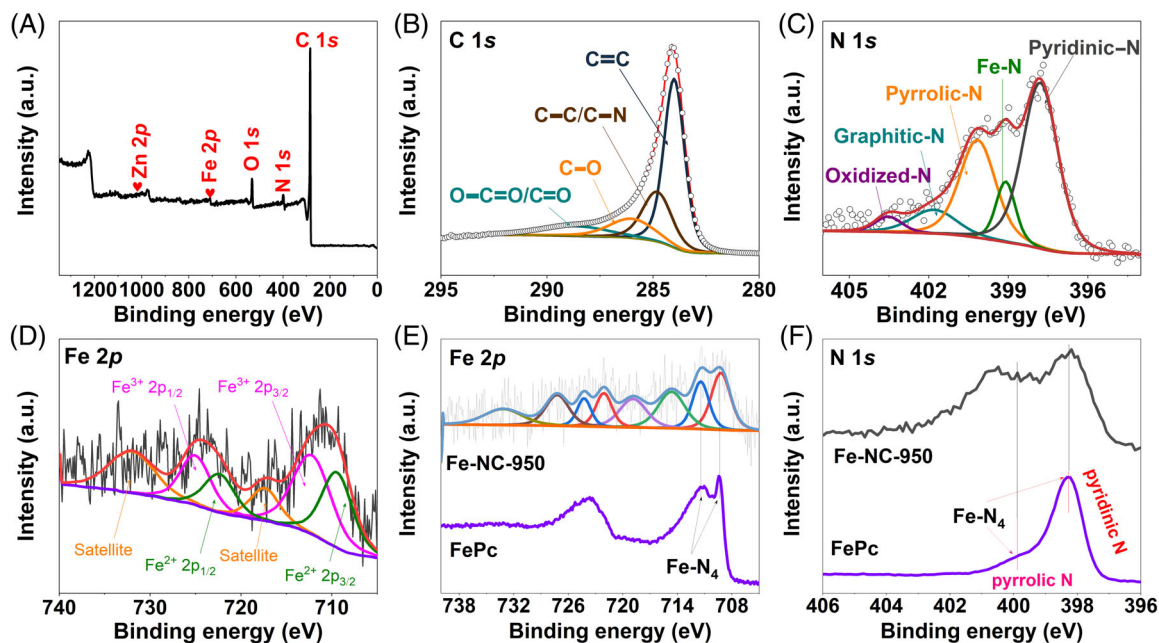
FIGURE 3 A, X-ray photoelectron spectroscopy (XPS) survey spectrum of Fe-NC-950. High-resolution XPS spectra of (B), C 1*s*, (C), N 1*s*, and (D), Fe 2*p* of Fe-NC-950. E, High-resolution XPS Fe 2*p* curves of Fe-NC-950 etched by 5 M HCl and FePc and F, high-resolution XPS N 1*s* curves of Fe-NC-950 etched by 5 M HCl and FePc

electrocatalytic activity of Fe-NC-950. As shown in Figure 3D, the high-resolution Fe 2*p* spectrum showed several deconvoluted peaks. Two peaks at 709.4 and 722.4 eV correspond to Fe^{2+} $2p_{3/2}$ and Fe^{2+} $2p_{1/2}$, while another pair of peaks at 712.2 and 725.0 eV corresponds to $2p_{3/2}$ and $2p_{1/2}$ of Fe^{3+} components, together with the binding energies at 717.4 and 732.0 eV were derived from satellite peaks. In particular, the affluent Fe^{2+} content was contributed by Fe-N species together with Fe^{2+} in the Fe oxide components.[69] The high-resolution Fe 2p spectrum of the control Fe-NC-1050 is shown in Figure S5, where the deconvoluted peaks of Fe^{3+}, Fe^{2+}, and Fe^{0} further demonstrate the existence of Fe_2O_3, FeO, and Fe components. Besides, the high-resolution Zn 2*p* has two typical peaks at 1021.1 and 1044.1 eV (Figure S6), which are attributed to the $2p_{3/2}$ and $2p_{1/2}$ electronic states of Zn^{2+}, respectively. As the metallic Zn evaporates, the remaining Zn is in the form of Zn-N.[70]

To investigate the dispersion level of the iron species, we conducted the following experiments. Firstly, we have impregnated the as-prepared Fe-NC-950 with 5 M HCl to remove Fe3O4. Further, we performed high-resolution transmission electron microscopy (HR-TEM) and EDS-mapping characterization, respectively. The XRD analysis confirmed the absence of any characteristic diffraction peaks of Fe_3O_4 in the pattern of Fe-NC-950 after acid treatment, which is preliminary proof that Fe_3O_4 is etched (the XRD pattern is shown in Figure S7). No lattice fringes are observed in the HR-TEM images of many

different areas (Figure S8a-j), proving Fe_3O_4 is removed. Meanwhile, EDS-mapping detects Fe′s sparse and scattered signal (Figure S8k). These manifest the isolated characteristic of Fe. In addition, it was also analyzed by XPS. Figure 3E shows the high-resolution Fe 2*p* spectra of the catalyst and iron phthalocyanine (FePc). The binding energies of the two characteristic peaks of Fe-N_4 in FePc correspond precisely to that of the catalyst. Figure 3F displays the high-resolution N 1*s* of the catalyst and FePc. The catalyst exhibits Fe-N_4-related peak positions that are consistent with FePc. Therefore, the results indicate that the iron species are dispersed throughout the catalyst at the atomic level.[71]

3.2 | Electrochemical evaluation for ORR

ORR performance of the electrocatalysts is investigated in O_2 or N_2 saturated 0.1 M KOH with RDE and RRDE techniques. The pyrolysis temperature endows the material with different catalytic properties. The RDE linear sweep voltammetry (LSV) curve of Fe-NC-950 obtained by pyrolyzing Fe-ZIF-8 at 950°C possesses the most positive $E_{1/2}$ and the maximum limiting current density (J_L) (Figure S9), showing 950°C was the optimum temperature. This can be attributed to the synergistically enhancing catalytic performance caused by the coexistence of
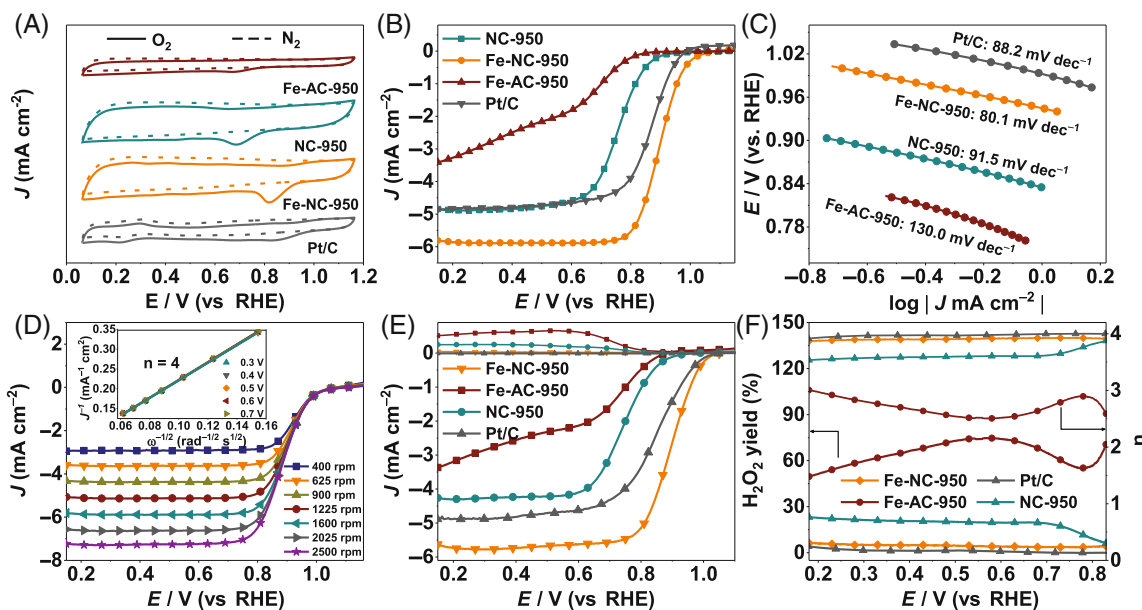
FIGURE 4 A, Cyclic voltammetry curves of Fe-NC-950, NC-950, Fe-AC-950, and Pt/C. B, rotating disk electrode (RDE) linear sweep voltammetry (LSV) curves, and C, Tafel plots of Fe-NC-950, NC-950, Fe-AC-950, and Pt/C. D, RDE LSV curves of Fe-NC-950 at varied rotation speed and the inset: corresponding Kouteckey-Levich fitting plots. E, Rotating ring-disk electrode LSV curves at 1600 rpm and F, the derived electron-transfer number n and H_2O_2 yield of Fe-NC-950, NC-950, Fe-AC-950 and Pt/C. All tests are in 0.1 M KOH

Fe_3O_4 and $Fe-N_x$ components. Hence, the catalysts discussed were prepared at 950°C.

The cyclic voltammetry (CV) curves of Fe-NC-950 catalyst together with NC-950, Fe-AC-950, and commercial Pt/C (20% Pt/C) are shown in Figure 4A. Fe-NC-950 displayed a more positive cathodic ORR reduction peak at 0.82 V than NC-950 and Fe-AC-950, but slightly higher than Pt/C due to the different catalyst properties and solute diffusion control process. The corresponding RDE LSV curves in Figure 4B showed the desirable activity of Fe-NC-950 with an $E_{1/2}$ of 0.89 V and a high E_{onset} of 1.04 V (defined as the potential at 0.1 mA cm^{-2}), surpassing that of commercial Pt/C (E_{onset} = 0.86 V). In addition, the J_L of Fe-NC-950 (5.90 mA cm^{-2}) surpassed that of Pt/C. Compared with the poor performance of Fe-free NC-950 and activated carbon-supported Fe-containing Fe-AC-950, Fe doping and ZIF-8 derived carbon support both were crucial to enhance catalytic activity, which might be related to the construction of more active $Fe-N_x$ and Fe_3O_4 sites compared with metal-free C-N$_x$ sites,[72,73] as well as the peculiarity of ZIF-8 derived carbon support. Compared with the recently reported catalysts, Fe-NC-950 showed better performance (Table S2). Moreover, the smaller Tafel slope of Fe-NC-950 (80.1 mV dec^{-1} vs 88.2 mV dec^{-1} for Pt/C, 91.5 mV dec^{-1} for NC-950, and 130.0 mV dec^{-1} for Fe-AC-950) was additional proof for better ORR activity, which also implied that the Fe-NC-950 catalyst possessed more desirable reaction kinetics (Figure 4C). For more insights into the reaction

mechanism of these catalysts, the RDE LSV plots were obtained at various rotating rates from 400 to 2500 rpm. The LSV curves of Fe-NC-950 are given in Figure 4D; the inset illustrates the corresponding excellent linearity Koutecky-Levich (K-L) plots, representing the numbers of electrons transferred per oxygen molecule in the reaction were nearly the same.[74] The average electron-transfer number of Fe-NC-950 was approximately 4 as evaluated by using K-L plots, suggesting it follows a four-electron ORR reaction process consistent with Pt/C. Likewise, the electron-transfer number of NC-950 and Fe-AC-950 were investigated, as shown in Figure S10a,b. The numbers of 3.4 for NC-950 and 3.1 for Fe-AC-950 portend the dissatisfactory four-electron ORR reaction mechanism. The RRDE LSV measurements were carried out to further verify the ORR reaction process (Figure 4E). A lower H_2O_2 yield (ca. 5%) and an electron-transfer number close to four over Fe-950-NC at the whole potential range confirmed a strong selectivity for four-electron ORR and a high ORR catalytic efficiency (Figure 4F).

Electrochemical double-layer capacitance (C_{dl}) can be devoted to evaluating the effective electrode-electrolyte interface area,[75] which can further estimate the ECSA and the quantity of available active centers exposed per unit area of the electrode. As ECSA is proportional to C_{dl}, meaning the higher the C_{dl} values, the higher the ECSA values, which is propitious for exposing more available active sites.[76] C_{dl} was calculated via a series of CVs with

FIGURE 5 A, Linear relationship diagram derived from $K_3[Fe(CN)_6]$ tests of Fe-NC-950, NC-950, and Fe-AC-950. B, Poison experiment by 0.1 mol L^{-1} KOH solution with 10 mM SCN⁻ of NC-950. C, Chronoamperometric response of Fe-NC-950 and Pt/C in the presence of 3 M methanol at a rotating speed of 1600 rpm. D, Chronoamperometric response of Fe-NC-950 and Pt/C. RHE, reversible hydrogen electrode (RHE)
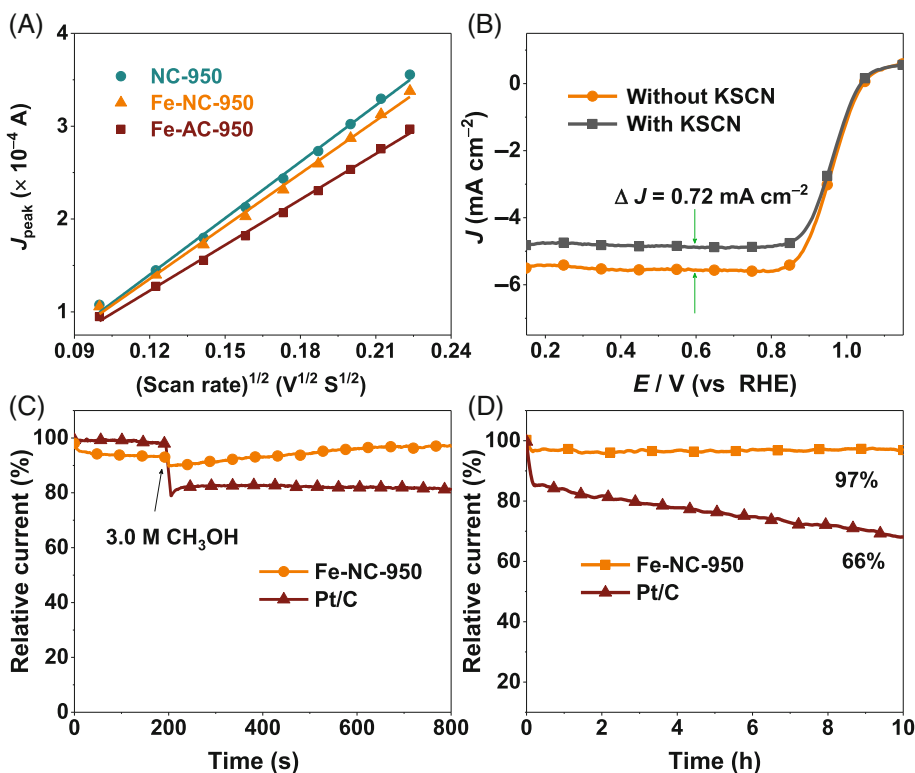
low sweeping rates from 4 to 40 mV s⁻¹ in 0.12-0.24 V vs reversible hydrogen electrode (RHE) (Figure S11a-c). In Figure S11d, the calculated specific C_{dl} value of Fe-NC-950 is 25.13 mF cm⁻² relative to that of NC-950 (27.05 mF cm⁻²) and Fe-AC-950 (5.55 mF cm⁻²). To assess actual ECSA values, a series of CVs in 10 mM $K_3[Fe(CN)_6]$ + 0.1 M KCl solution with a sweeping rate from 10 to 50 mV s⁻¹ in 0.1 to 0.5 V vs Ag/AgCl was performed (Figure S12a-c). As shown in Figure 5A, the corresponding redox peaks present an excellent linearity vs the square root of the sweeping rates, and the ECSA values were positively correlated to the slope. It was observed that Fe-NC-950 has lower ECSA value than NC-950, but had higher ORR activity than NC-950. This manifests that ECSA value was just a factor that affects catalytic activity. However, introducing iron species with intrinsic catalytic activity was the key to advancing the ORR performance.

Thanks to the strong sensitivity and reactivity of SCN⁻ to transition metals, the SCN⁻ coordinated with metallic species intensely in carbon or graphene-based materials could significantly restrain the absorption of O_2 onto the metal center.[74,77] Hence, to directly find out the effect of Fe-Nₓ, SCN⁻ ions, poisoning experiment was performed in the presence of 10 mM KSCN. A significant drop of J_L (0.72 mA cm⁻²) on LSV curves after 10 mM KSCN addition was observed (Figure 5B), signifying a strong SCN⁻ ion coordination and impediment of the active Fe-Nₓ centers. Confirming the Fe-Nₓ moieties

played a positive role in enhancing ORR activity. The same SCN⁻ ions poisoning experiment was performed on the Fe-free catalyst (NC-950) to explain further whether the residual Zn species influences ORR. After the poisoning test, the ORR activity of NC-950 did not decrease, signifying that the effect of a single Zn species on ORR activity was negligible (Figure S13). According to previous reports, the composite of Fe_3O_4 and N-doped carbon materials was an effective way to prepare catalysts with high oxygen reduction activity.[72,78] The Fe_3O_4 leaching experiment of Fe-NC-950 was performed by soaking in 5 M hydrochloric acid, as shown in Figure S14. When the Fe_3O_4 moieties were removed (XRD pattern in Figure S7), the $E_{1/2}$ negatively shifted 0.20 V of Fe-NC-950. As discussed above, we believe Fe-Nₓ and Fe_3O_4 were the main active sites of Fe-NC-950. The result suggested that the excellent activity of Fe-NC-950 might originate from the synergistic effect of Fe-Nₓ and Fe_3O_4 moieties.[56]

The durability of Fe-NC-950 was assessed through chronoamperometry and CVs. Figure 5C shows that Fe-NC-950 retained up to 97% of the initial current density after operating for 36 000 seconds while only 66% of current was retained for Pt/C. The CVs measurement runs within the potential of −0.9 to 0.1 V vs Ag/AgCl in sweeping rate of 100 mV s⁻¹ at 1600 rpm. The Fe-NC-950 demonstrated a modest decay of 0.50 mA cm⁻² in limiting current density and an indistinguishable change in $E_{1/2}$ after 2000 cycles, which may be inevitably effect the
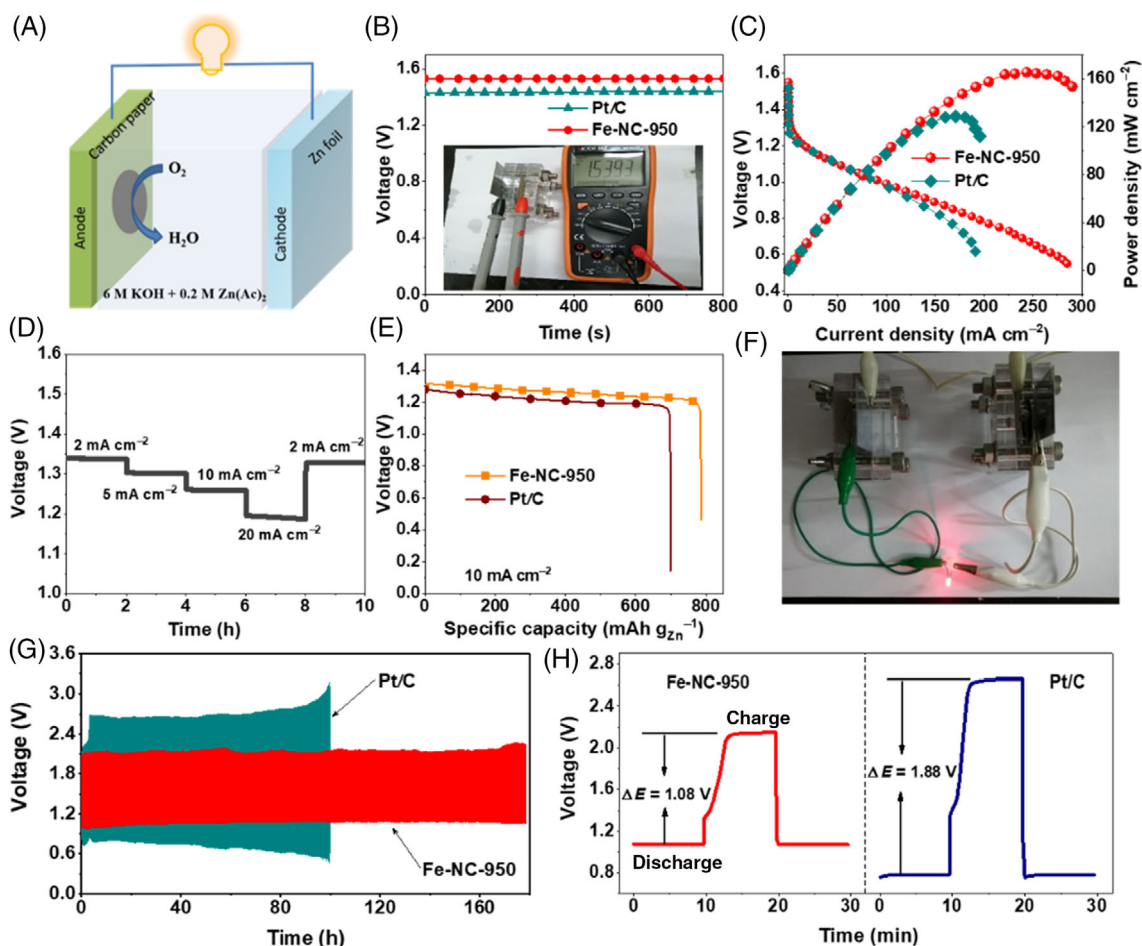
FIGURE 6 A, Sketch diagram of zinc-air battery device. B, Open-circuit voltage of Pt/C and Fe-NC-950 based zinc-air batteries. C, *V-i* polarization and corresponding power density profiles. D, Discharge curves of the zinc-air batteries at different current densities. E, Specific capacity of Pt/C and Fe-NC-950 based zinc-air batteries. F, Photographs of a lighted light-emitting diode (~3 V) powered by two series of batteries. G, Galvanostatic charge and discharge cycling curves at a current density of 10 mA cm^{-2}. H, Partial enlarged view of galvanostatic charge and discharge cycling curves

slight shedding of the catalyst under highly speed rotation (Figure S15). Thus, suggesting the satisfactory ORR durability of Fe-NC-950 that is beyond Pt/C. In addition, unlike Pt/C, Fe-NC-950 also showed excellent tolerance to methanol (Figure 5D).

3.3 | Zn-air battery performance

To further explore the real-world application of the Fe-NC-950, an integrated rechargeable zinc-air battery was fabricated and investigated. Figure 6A shows a schematic diagram of a homemade rechargeable zinc-air battery. Figure 6B shows the Fe-NC-950-based battery achieving a high OCV of 1.54 V, which was higher than that of Pt/C-based battery (1.44 V). The Fe-NC-950-based battery provides a peak power density of 165.0 mW cm^{-2} at 242 mA cm^{-2}, outperforming Pt/C-based zinc-air battery

(128 mW cm^{-2}), manifesting a superiority of Fe-NC-950 in application aspect (Figure 6C). Moreover, Fe-NC-950 equipped battery showed stable voltage platforms at various discharge current densities (Figure 6D). The steady discharge voltage and no significant degradation of Fe-NC-950-based battery was confirmed by the galvanostatic discharge curve at 10 mA cm^{-2} (Figure 6E). The specific capacity for the Fe-NC-950-based battery reaches 786.7 mA h g$_{Zn}^{-1}$ at 10 mA cm^{-2}, while the Pt/C-based battery just outputs a specific capacity of 698 mA h g$_{Zn}^{-1}$. Compared with recently reported advanced catalysts (Table S3), Fe-NC-950-based battery also exhibits better performance. With two zinc-air batteries in series, a light-emitting diode can be easily lit (Figure 6F). The OER performance of Fe-NC-950 shown by the polarization curve after *iR* correction (Figure S16) implies the rechargeability of the Fe-NC-950-based battery. The consecutive charge-discharge profiles of the Fe-NC-

950-based battery were identical even after 170 hours (510 cycles) cycling test, featuring a favorable cycling stability (Figure 6G). Under the same condition, Pt/C-based battery presented the stable cycling only for 100 hours (300 cycles). From the enlarged cycling curves (Figure 6H), the Fe-NC-950-based battery showed a lower voltage gap of 1.08 V than that of Pt/C-based battery (1.88 V). A depressed voltage gap was critical to ensure the stable cycling of rechargeable zinc-air battery. These results manifested the promising performance of Fe-NC-950 in zinc-air battery application.

3.4 | Mechanism analysis

The above experimental results confirm that the dual-site catalyst has excellent oxygen reduction performance in an alkaline medium, attributed to the following aspects. (a) Formation of nitrogen-doped carbon supports mesoporous and unique stereo-geometric properties to facilitate the diffusion of O_2 and electrolytes and improve the utilization of internal active sites. (b) Generally, Fe atoms coordinate with pyridine-N to form Fe-N_x active sites, and higher pyridine nitrogen content (48.7%) in Fe-NC-950 is beneficial to form more active sites.[50] (c) Three types of mechanisms of ORR are as follows: (a) *O_2 dissociation pathway; (b) *OOH dissociation pathway; and (c) *HOOH dissociation pathway.[79,80] Previous DFT study suggested that the *OOH dissociation pathway is the kinetically most favorable one for the ORR on Fe-N_x sites.[49] Combined with our experiments, we believe that Fe-N_x is the main active site and follows the *OOH dissociation mechanism. Firstly, the O_2 molecule is adsorbed on the Fe site of Fe-N_x, followed by a hydrogenation reaction to form an adsorbed *OOH molecule. Secondly, the O—O bond in *OOH splits to produce an *O atom adsorbed on Fe site and an *OH molecule adsorbed on the top of an adjacent C atom. Thirdly, the *O atom undergoes sequential hydrogenation reactions to form the first H_2O molecule and is released, whereas the *OH molecule will migrate to the Fe site to generate the second H_2O molecule through a hydrogenation reaction. The rate-determining step *OOH dissociated to form *O and *OH. Fe_3O_4 species activated around Fe-N_x, decreasing the adsorption free energy of Fe-N_x sites for O_2 molecules,[51] which can increase the reactant concentration for ORR. Therefore, Fe_3O_4 and Fe-N_x synergistically strengthened the O_2 adsorption, enhancing the overall activity.

4 | CONCLUSION

In summary, the coexisting Fe_3O_4 and Fe-N_x active sites were fabricated as new synergistically enhanced active

sites for energy conversion. The combination of Fe_3O_4 and Fe-N_x dual active sites has been achieved. The ZIF-8-derived N-doped carbon substrate with a large specific surface area and unique three-dimensional structure facilitated the transmission of electrons and dispersion of active sites. Pyrolysis experiments proved a direct transformation of iron species into Fe_3O_4 and Fe-N_x without forming unstable components under 950°C. Because of their architectural and compositional merits, such an as-prepared catalyst with Fe_3O_4 and Fe-N_x dual active site displayed satisfactory catalytic ORR performance, superior tolerance toward methanol crossover, and impressive durability, surpassing the Pt/C benchmark. Experimental results revealed that Fe_3O_4 and Fe-N_x are the main origins of the high catalytic activity. The residual Zn species inherited from ZIF had no impact on the catalyst performance. The high catalytic activity stems from the two key areas: (a) ZIF-8-derived N-doped carbon as unique support provides large ECSA, increases the conductivity, and accelerates the mass transfer, which was the precondition; (b) The possible synergistic effect between Fe_3O_4 and Fe-N_x gained the enhanced ORR activity. This work provides a workable pathway for designing efficient non-precious-metal ORR catalysts in the application of zinc-air batteries.

DATA AVAILABILITY STATEMENT
We state that all data is available.

ORCID
Xiulin Yang https://orcid.org/0000-0003-2642-4963

REFERENCES

1. Chen SM, Cheng JY, Ma LT, et al. Light-weight 3D Co-N-doped hollow carbon spheres as efficient electrocatalysts for rechargeable zinc-air batteries. *Nanoscale*. 2018;10:10412-10419.
2. Tahir M, Pan L, Idrees F, et al. Electrocatalytic oxygen evolution reaction for energy conversion and storage: a comprehensive review. *Nano Energy*. 2017;37:136-157.
3. Suen NT, Hung SF, Quan Q, Zhang N, Xu YJ, Chen HM. Electrocatalysis for the oxygen evolution reaction: recent development and future perspectives. *Chem Soc Rev*. 2017;46:337-365.
4. Seh ZW, Kibsgaard J, Dickens CF, Chorkendorff I, Nørskov JK, Jaramillo TF. Combining theory and experiment in electrocatalysis: insights into materials design. *Science*. 2017;355:1-33.

5. Fu J, Paul-Cano Z, Gyu-Park M, Yu AP, Fowler M, Chen ZW. Electrically rechargeable zinc-air batteries: progress, challenges, and perspectives. *Adv Mater*. 2017;29:1604685.

6. Shah SSA, Najam T, Aslam MK, et al. Recent advances on oxygen reduction electrocatalysis: correlating the characteristic properties of metal organic frameworks and the derived nanomaterials. *Appl Catal Environ*. 2020;268:118570.

7. Kwak WJ, Rosy SD, Xia C, et al. Lithium-oxygen batteries and related systems: potential, status, and future. *Chem Soc Rev*. 2020;120:6626-6683.

8. Zitolo A, Goellner V, Armel V, et al. Identification of catalytic sites for oxygen reduction in iron- and nitrogen-doped graphene materials. *Nat Mater*. 2015;14:937-942.

9. Tang C, Wang HF, Zhang Q. Multiscale principles to boost reactivity in gas-involving energy electrocatalysis. *Acc Chem Res*. 2018;51:881-889.

10. Chen YJ, Ji SF, Wang YG, et al. Isolated single iron atoms anchored on N-doped porous carbon as an efficient electrocatalyst for the oxygen reduction reaction. *Angew Chem Int Ed*. 2017;56:6937-6941.

11. Jia Y, Zhang LZ, Zhuang LZ, et al. Identification of active sites for acidic oxygen reduction on carbon catalysts with and without nitrogen doping. *Nat Catal*. 2019;2:688-695.

12. Wang J, Huang ZQ, Liu W, et al. Design of N-coordinated dual-metal sites: a stable and active Pt-free catalyst for acidic oxygen reduction reaction. *J Am Chem Soc*. 2017;139:17281-17284.

13. Zhang LZ, Agatha-Fischer JMT, Jia Y, et al. Coordination of atomic Co-Pt coupling species at carbon defects as active sites for oxygen reduction reaction. *J Am Chem Soc*. 2018;140:10757-10763.

14. Ban JJ, Wen XH, Xu HJ, et al. Dual evolution in defect and morphology of single-atom dispersed carbon based oxygen electrocatalyst. *Adv Funct Mater*. 2021;31:2010472.

15. Li J, Chen SG, Yang N, et al. Ultrahigh-loading zinc single-atom catalyst for highly efficient oxygen reduction in both acidic and alkaline media. *Angew Chem Int Ed*. 2019;58:7035-7039.

16. Liu MJ, Lee JY, Yang TC, et al. Synergies of Fe single atoms and clusters on N-doped carbon electrocatalyst for pH-universal oxygen reduction. *Small Methods*. 2021;5:2001165.

17. Han YH, Wang YG, Luo J, et al. Hollow N-doped carbon spheres with isolated cobalt single atomic sites: superior electrocatalysts for oxygen reduction. *J Am Chem Soc*. 2017;139:17269-17272.

18. Zhu CZ, Fu SF, Song JH, et al. Self-assembled Fe-N-doped carbon nanotube aerogels with single-atom catalyst feature as high-efficiency oxygen reduction electrocatalysts. *Small*. 2017;13:1603407.

19. Wu Q, Yang LJ, Wang XZ, Hu Z. From carbon-based nanotubes to nanocages for advanced energy conversion and storage. *Acc Chem Res*. 2017;50:435-444.

20. Zhou RF, Zheng Y, Jaroniec M, Qiao SZ. Determination of the electron transfer number for the oxygen reduction reaction: from theory to experiment. *ACS Catal*. 2016;6:4720-4728.

21. Wu G, Santandreu A, Kellogg W, et al. Carbon nanocomposite catalysts for oxygen reduction and evolution reactions: from nitrogen doping to transition-metal addition. *Nano Energy*. 2016;29:83-110.

22. Yin PQ, Yao T, Wu YE, et al. Single cobalt atoms with precise N-coordination as superior oxygen reduction reaction catalysts. *Angew Chem Int Ed*. 2016;55:10800-10805.

23. Zhang JT, Zhao ZH, Xia ZH, Dai LM. A metal-free bifunctional electrocatalyst for oxygen reduction and oxygen evolution reactions. *Nat Nanotechnol*. 2015;10:444-452.

24. Yuan K, Lu CB, Sfaelou S, et al. In situ nanoarchitecturing and active-site engineering toward highly efficient carbonaceous electrocatalysts. *Nano Energy*. 2019;59:207-215.

25. Zhao YS, Wan JW, Yao HY, et al. Few-layer graphdiyne doped with sp-hybridized nitrogen atoms at acetylenic sites for oxygen reduction electrocatalysis. *Nat Chem*. 2018;10:924-931.

26. Liu D, Dai LM, Lin XN, et al. Chemical approaches to carbon-based metal-free catalysts. *Adv Mater*. 2019;31:1804863.

27. Yang LJ, Shui JL, Du L, et al. Carbon-based metal-free ORR electrocatalysts for fuel cells: past, present, and future. *Adv Mater*. 2019;31:1804799.

28. Liu X, Dai LM. Carbon-based metal-free catalysts. *Nat Rev Mater*. 2016;1:16064.

29. Guo DH, Shibuya R, Akiba C, Saji S, Kondo T, Nakamura J. Active sites of nitrogen-doped carbon materials for oxygen reduction reaction clarified using model catalysts. *Science*. 2016;351:361-365.

30. Chung HT, Cullen DA, Higgins D, et al. Direct atomic-level insight into the active sites of a high-performance PGM-free ORR catalyst. *Science*. 2017;357:479-484.

31. Li JZ, Chen MJ, Cullen DA, et al. Atomically dispersed manganese catalysts for oxygen reduction in proton-exchange membrane fuel cells. *Nat Catal*. 2018;1:935-945.

32. Kulkarni A, Siahrostami S, Patel A, Nørskov JK. Understanding catalytic activity trends in the oxygen reduction reaction. *Chem Rev*. 2018;118:2302-2312.

33. Li JK, Jaouen F. Structure and activity of metal-centered coordination sites in pyrolyzed metal–nitrogen–carbon catalysts for the electrochemical reduction of O_2. *Curr Opin Electrochem*. 2018;9:198-206.

34. Wang W, Jia QY, Mukerjee S, Chen SL. Recent insights into the oxygen-reduction electrocatalysis of Fe/N/C materials. *ACS Catal*. 2019;9:10126-10141.

35. Zhu YZ, Sokolowski J, Song XC, He YH, Mei Y, Wu G. Engineering local coordination environments of atomically dispersed and heteroatom-coordinated single metal site electrocatalysts for clean energy-conversion. *Adv Energy Mater*. 2019;10:1902844.

36. Su PP, Xiao H, Zhao J, et al. Nitrogen-doped carbon nanotubes derived from Zn–Fe-ZIF nanospheres and their application as efficient oxygen reduction electrocatalysts with in situ generated iron species. *Chem Sci*. 2013;4:2941-2946.

37. Strickland K, Miner E, Jia QY, et al. Highly active oxygen reduction non-platinum group metal electrocatalyst without direct metal-nitrogen coordination. *Nat Commun*. 2015;6:7343.

38. Huang XQ, Wu XJ, Niu YL, Dai CL, Xu MW, Hu WH. Effect of nanoparticle composition on oxygen reduction reaction activity of Fe/N–C catalysts: a comparative study. *Cat Sci Technol*. 2019;9:711-717.

39. Ye YF, Cai F, Li HB, et al. Surface functionalization of ZIF-8 with ammonium ferric citrate toward high exposure of Fe-N active sites for efficient oxygen and carbon dioxide electroreduction. *Nano Energy*. 2017;38:281-289.

40. Gupta S, Zhao S, Ogoke O, Lin Y, Xu H, Wu G. Engineering favorable morphology and structure of Fe-N-C oxygen-reduction catalysts through tuning of nitrogen/carbon precursors. *ChemSusChem*. 2017;10:774-785.

41. Xiao ML, Zhu JB, Li GR, et al. A single-atom iridium heterogeneous catalyst in oxygen reduction reaction. *Angew Chem Int Ed*. 2019;58:9640-9645.

42. Zhang HG, Sy H, Wang MY, et al. Single atomic iron catalysts for oxygen reduction in acidic media: particle size control and thermal activation. *J Am Chem Soc*. 2017;139:14143-14149.

43. Sheng S, Liu W, Zhu K, et al. Fe_3O_4 nanospheres in situ decorated graphene as high-performance anode for asymmetric supercapacitor with impressive energy density. *J Colloid Interface Sci*. 2019;536:235-244.

44. Suarez SME, Borja-Castro LE, Valerio-Cuadros MI, et al. Carbothermal reduction of mill scales formed on steel billets during continuous casting. *Hyperfine Interact*. 2021;242:29.

45. Wang ZQ, Deng SH, Zhang QY, Li JZ, Lin QL. Effects of carbothermal reduction of iron oxide on microstructures and electrochemical properties of the carbon foams. *J Alloys Compd*. 2022;890:161804.

46. Afsahi F, Kaliaguine S. Non-precious electrocatalysts synthesized from metal–organic frameworks. *J Mater Chem A*. 2014;2:12270-12279.

47. Proietti E, Jaouen F, Lefevre M, et al. Iron-based cathode catalyst with enhanced power density in polymer electrolyte membrane fuel cells. *Nat Commun*. 2011;2:416.

48. Yuan K, Lützenkirchen-Hecht D, Li LB, et al. Boosting oxygen reduction of single iron active sites via geometric and electronic engineering: nitrogen and phosphorus dual coordination. *J Am Chem Soc*. 2020;142:2404-2412.

49. Kattel S, Wang GF. Reaction pathway for oxygen reduction on FeN_4 embedded graphene. *J Phys Chem Lett*. 2014;5:452-456.

50. Zhao XL, Yang XX, Wang MY, et al. Single-iron site catalysts with self-assembled dual-size architecture and hierarchical porosity for proton-exchange membrane fuel cells. *Appl Catal Environ*. 2020;279:119400.

51. Hu SQ, Ni WP, Yang DH, et al. Fe_3O_4 nanoparticles encapsulated in single-atom Fe–N–C towards efficient oxygen reduction reaction: effect of the micro and macro pores. *Carbon*. 2020;162:245-255.

52. Yang ZK, Yuan C-Z, Xu A-W. Confined pyrolysis within a nanochannel to form a highly efficient single iron site catalyst for Zn–air batteries. *ACS Energy Lett*. 2018;3:2383-2389.

53. Wu ZX, Li W, Xia YY, Webley P, Zhao DY. Ordered mesoporous graphitized pyrolytic carbon materials: synthesis, graphitization, and electrochemical properties. *J Mater Chem A*. 2012;22:8835-8845.

54. Lin L, Zhu Q, Xu A-W. Noble-metal-free Fe–N/C catalyst for highly efficient oxygen reduction reaction under both alkaline and acidic conditions. *J Am Chem Soc*. 2014;136:11027-11033.

55. Li LJ, Dai PC, Gu X, Wang Y, Yan LT, Zhao XB. High oxygen reduction activity on a metal–organic framework derived carbon combined with high degree of graphitization and pyridinic-N dopants. *J Mater Chem A*. 2017;5:789-795.

56. Guo JN, Cheng YH, Xiang ZH. Confined-space-assisted preparation of Fe_3O_4-nanoparticle-modified Fe–N–C catalysts derived from a covalent organic polymer for oxygen reduction. *ACS Sustain Chem Eng*. 2017;5:7871-7877.

57. Tang C, Zhang Q. Nanocarbon for oxygen reduction electrocatalysis: dopants, edges, and defects. *Adv Mater*. 2017;29:1604103.

58. Jiang H, Gu JX, Zheng XS, et al. Defect-rich and ultrathin N doped carbon nanosheets as advanced trifunctional metal-free electrocatalysts for the ORR, OER and HER. *Energ Environ Sci*. 2019;12:322-333.

59. Li DH, Jia Y, Chang GJ, et al. A defect-driven metal-free electrocatalyst for oxygen reduction in acidic electrolyte. *Chem*. 2018;4:2345-2356.

60. Wang JW, Jia ZR, Liu XH, et al. Construction of 1D Heterostructure NiCo@C/ZnO nanorod with enhanced microwave absorption. *Nano-Micro Lett*. 2021;13:175.

61. Zhao HY, Sun CH, Jin Z, et al. Carbon for the oxygen reduction reaction: a defect mechanism. *J Mater Chem A*. 2015;3:11736-11739.

62. Gong XF, Zhu JB, Li JZ, et al. Self-templated hierarchically porous carbon nanorods embedded with atomic $Fe-N_4$ active sites as efficient oxygen reduction electrocatalysts in Zn-air batteries. *Adv Funct Mater*. 2021;31:2008085.

63. Zhou YZ, Chen GB, Wang Q, et al. Fe-N-C electrocatalysts with densely accessible $Fe-N_4$ sites for efficient oxygen reduction reaction. *Adv Funct Mater*. 2021;31:2102420.

64. Xiao F, Xu G-L, Sun C-J, et al. Nitrogen-coordinated single iron atom catalysts derived from metal organic frameworks for oxygen reduction reaction. *Nano Energy*. 2019;61:60-68.

65. Liu XH, Zhai XW, Sheng WB, et al. Isolated single iron atoms anchored on a N, S-codoped hierarchically ordered porous carbon framework for highly efficient oxygen reduction. *J Mater Chem A*. 2021;9:10110-10119.

66. Yu DS, Goh K, Wang H, et al. Scalable synthesis of hierarchically structured carbon nanotube-graphene fibres for capacitive energy storage. *Nat Nanotechnol*. 2014;9:555-562.

67. Liu Y, Shen YT, Sun LT, et al. Elemental superdoping of graphene and carbon nanotubes. *Nat Commun*. 2016;7:10921.

68. Sakaushi K, Lyalin A, Tominaka S, Taketsugu T, Uosaki K. Two-dimensional corrugated porous carbon-, nitrogen-framework/metal heterojunction for efficient multielectron transfer processes with controlled kinetics. *ACS Nano*. 2017;11:1770-1779.

69. Serov A, Artyushkova K, Atanassov P. Fe-N-C oxygen reduction fuel cell catalyst derived from carbendazim: synthesis, structure, and reactivity. *Adv. Energy Mater*. 2014;4:1301735.

70. Qian M, Xu M, Guo M, et al. Synergistically catalytic enhanced of Zn–N/Co–N dual active sites as highly efficient and durable bifunctional electrocatalyst for rechargeable zinc-air battery. *J Power Sources*. 2021;506:230221.

71. Li J-C, Yang Z-Q, Tang D-M, et al. N-doped carbon nanotubes containing a high concentration of single iron atoms for efficient oxygen reduction. *NPG Asia Mater*. 2018;10:e461.

72. Wang Y, Wu MM, Wang K, Chen JW, Yu TW, Song SQ. Fe_3O_4@N-doped interconnected hierarchical porous carbon and its 3D integrated electrode for oxygen reduction in acidic media. *Adv Sci*. 2020;7:2000407.

73. Holby EF, Wu G, Zelenay P, Taylor CD. Structure of $Fe-N_x-C$ defects in oxygen reduction reaction catalysts from first-principles modeling. *J Phys Chem C*. 2014;118:14388-14393.

74. Wang ZH, Jin HH, Meng T, et al. Fe, cu-coordinated ZIF-derived carbon framework for efficient oxygen reduction reaction and zinc-air batteries. *Adv Funct Mater*. 2018;28:1802596.

75. Li JT, Huang WZ, Wang MM, et al. Low-crystalline bimetallic metal–organic framework electrocatalysts with rich active sites for oxygen evolution. *ACS Energy Lett*. 2019;4:285-292.

76. Sun JQ, Yang DJ, Lowe S, et al. Sandwich-like reduced graphene oxide/carbon black/amorphous cobalt borate nanocomposites as bifunctional cathode electrocatalyst in rechargeable zinc-air batteries. *Adv Energy Mater*. 2018;8: 1801495.

77. Liu QT, Liu XF, Zheng LR, Shui JL. The solid-phase synthesis of an Fe-N-C electrocatalyst for high-power proton-exchange membrane fuel cells. *Angew Chem Int Ed*. 2018;57:1204-1208.

78. Gao SY, Fan BF, Feng R, et al. N-doped-carbon-coated Fe_3O_4 from metal-organic framework as efficient electrocatalyst for ORR. *Nano Energy*. 2017;40:462-470.

79. Duan ZY, Wang GF. A first principles study of oxygen reduction reaction on a Pt(111) surface modified by a subsurface transition metal M (M = Ni, Co, or Fe). *Phys Chem Chem Phys*. 2011;13:20178-20187.

80. Wu L, Cao XR, Hu W, Ji YF, Zhu Z-Z, Li X-F. Improving the oxygen reduction reaction activity of FeN_4–graphene via tuning electronic characteristics. *ACS Appl Energy Mater*. 2019;2:6634-6641.

SUPPORTING INFORMATION

Additional supporting information may be found in the online version of the article at the publisher's website.